Chapter 2: Changes in Atmospheric Constituents and in Radiative Forcing

Coordinating Lead Authors: Piers Forster, V. Ramaswamy

Lead Authors: Paulo Artaxo, Terje Berntsen, Richard Betts, Dave Fahey, Jim Haywood, Judith Lean, Dave Lowe, Gunnar Myhre, John Nganga, Ronald Prinn, Graciela Raga, Michael Schulz, Rob Van Dorland

Contributing Authors: Greg Bodeker (NIWA), George Boer, Olivier Boucher, William Collins (NCAR), Thomas J. Conway (CMDL), Ed Dlugokencky (CMDL), Jim Elkins (CDML), David Etheridge (CSIRO), Paul Fraser (CSIRO), Dave Keeling (Scripps), Stefan Kinne, Keith Lassey (NIWA), Ulrike Lohmann (ZTH), Andrew Manning (UEA), Steve Montzka (CDML), David Oram (UEA), Kath O'Shaughnessy (NIWA), Steve Piper (Scripps), Michael Ponater (DLR), Navin Ramankutty, Karen Rosenlof (NOAA), Robert Sausen, M. D. Schwarzkopf (GFDL), Gera Stenchikov, Nicola Stuber (Reading), Christiane Textor, Ray Wang (GaTech), Ray Weiss (Scripps), Tim Whorf (Scripps)

Review Editors: Teruyuki Nakajima, V. Ramanathan

Date of Draft: 11 August 2005

Notes: This is the TSU compiled version

Figures

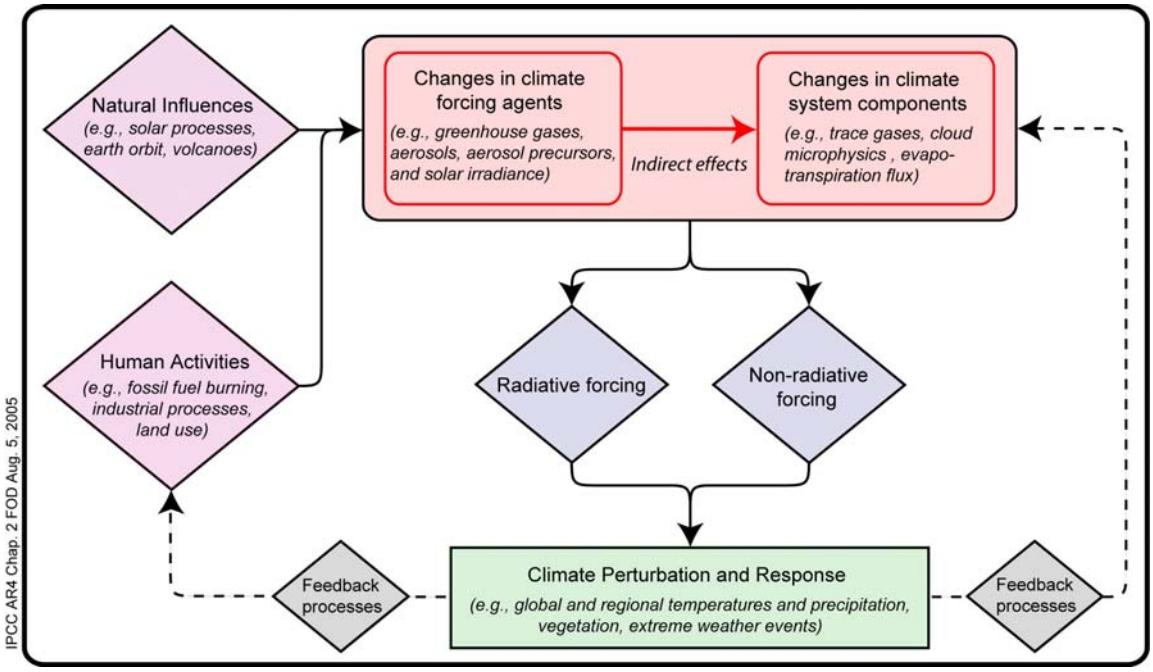

Figure 2.2.1. Flow diagram illustrating how RF links to other areas of climate change being assessed in this report.

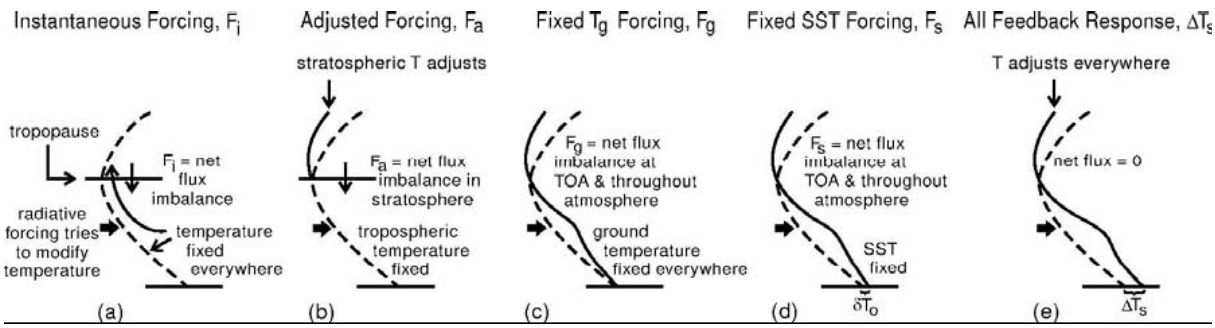

Figure 2.2.2. Cartoon comparing (a) F_i, instantaneous forcing, (b) F_a, adjusted forcing, which allows stratospheric temperatures to adjust, (c) F_g, fixed surface temperature forcing, which allows atmospheric temperatures to adjust, (d) F_s, fixed SST forcing, which allows both atmospheric temperatures and land temperatures to adjust, (e) ΔT_s, global surface air temperature calculated by the climate model in response to the forcing agent. From Hansen *et al.* (2005).

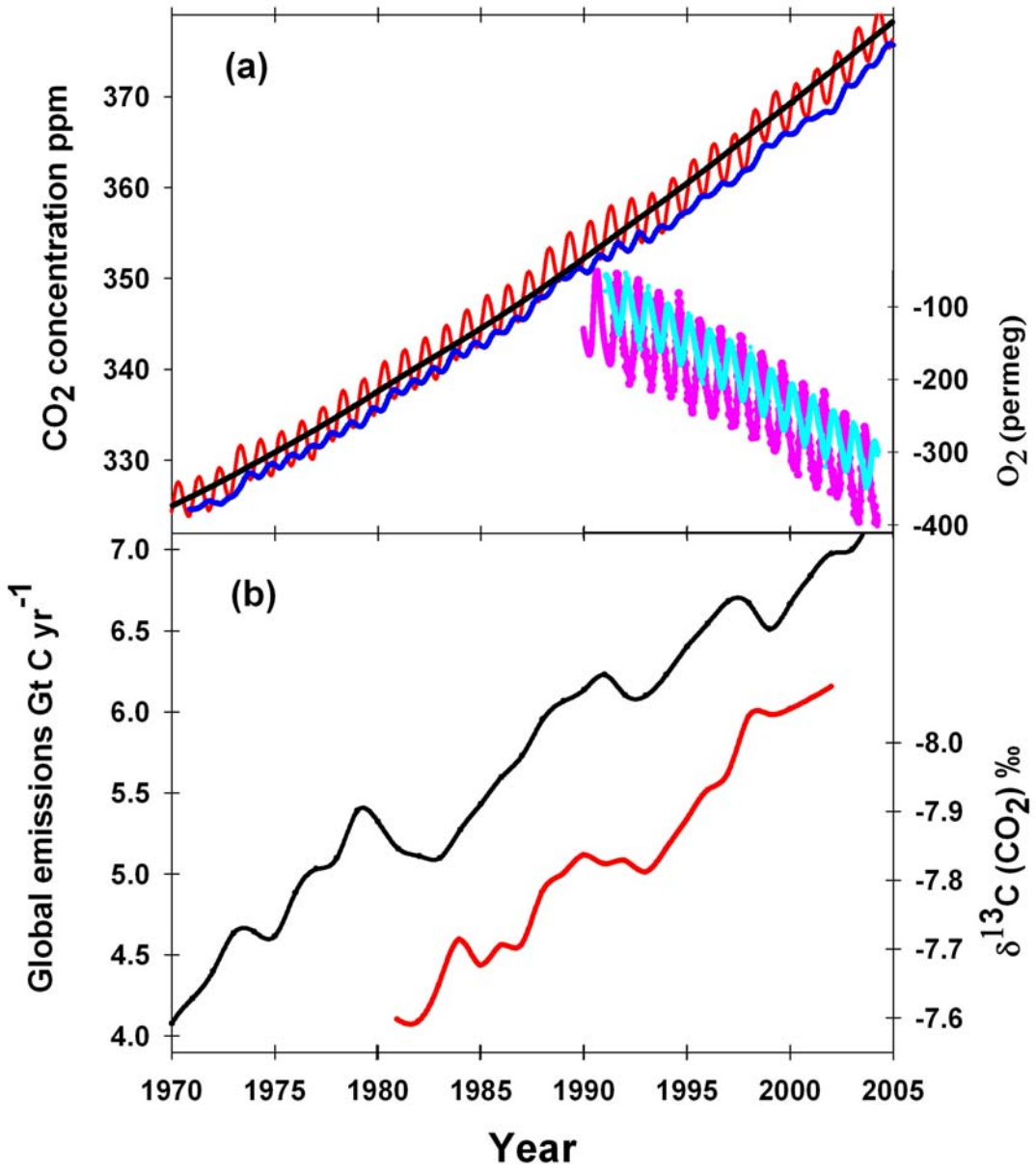

Figure 2.3.1 Panel (a) shows CO_2 concentrations (monthly averages) measured by continuous analyser over the period 1970 to 2004 for Mauna Loa, Northern Hemisphere (red) (Keeling and Whorf, 2005) and Baring Head, Southern Hemisphere (blue) (Manning *et al.,* 1997). Due to the larger amount of terrestrial biosphere in the Northern hemisphere, seasonal cycles in CO_2 are larger there than in the Southern hemisphere. The black line represents the cumulative fossil fuel emissions (Data from the CDIAC website (Marland *et al.*, 2005) fitted to the seasonally adjusted Mauna Loa CO_2 data with a constant airborne fraction of 57% (see text). In the lower right of the panel, atmospheric oxygen measurements are shown from Alert, Northern Hemisphere (pink) and Cape Grim (cyan) (Manning and Keeling, 2005).The oxygen data is given in "permeg" (parts per million) deviations from a calibration standard. Panel (b) shows the annual global CO_2 emissions from fossil-fuel burning, cement manufacture and gas flaring expressed as Gt C yr^{-1}(black) through to 2002 (Data from the CDIAC website (Marland *et al*, 2005). Preliminary emissions data for 2003 and 2004 of 7.0 and 7.2 Gt C yr^{-1} are added derived from British Petroleum (2005). Annual averages of the $^{13}C/^{12}C$ ratio measured in atmospheric CO_2 at Mauna Loa from 1981 to 2002 (red) are also shown (Keeling *et al*, 2005). The isotope data are expressed as $\delta^{13}C(CO_2)$ "‰" (parts per thousand) deviation from a calibration standard.

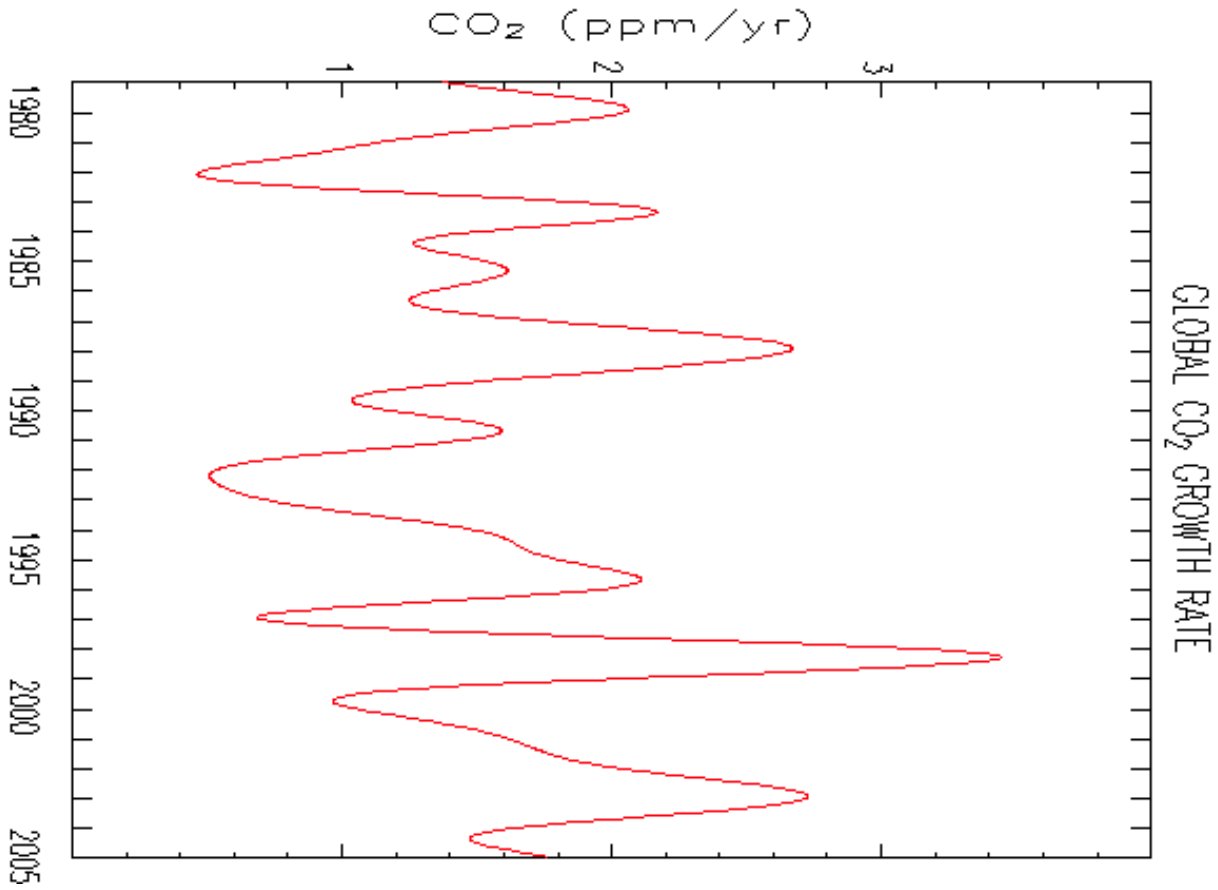

Figure 2.3.2 Annual growth rate (ppm yr^{-1}) in global atmospheric carbon dioxide from 1979 through 2003 calculated as the derivative of the deseasonalized trend curve in Figure 2.3.1 (a). The annual increases are from 1 January to 1 January the following year. [Uncertainties will be added.]

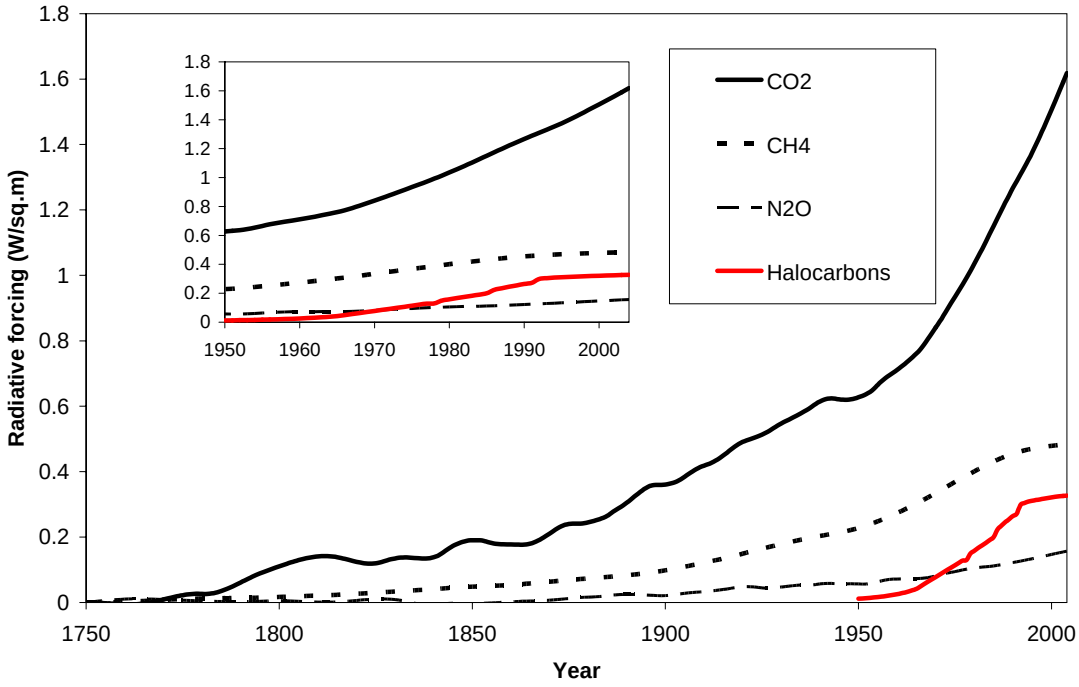

Figure 2.3.3. Timeseries of LLGHG radiative forcing constructed from observed gas concentrations. The concentrations are based on several datasets from ice-cores, firn air, flask an in-situ measurements discussed in Section 2.3, see also McFarling Meure (2004). A 20-year spline fit has been used for the non halocarbon gas concentrations.

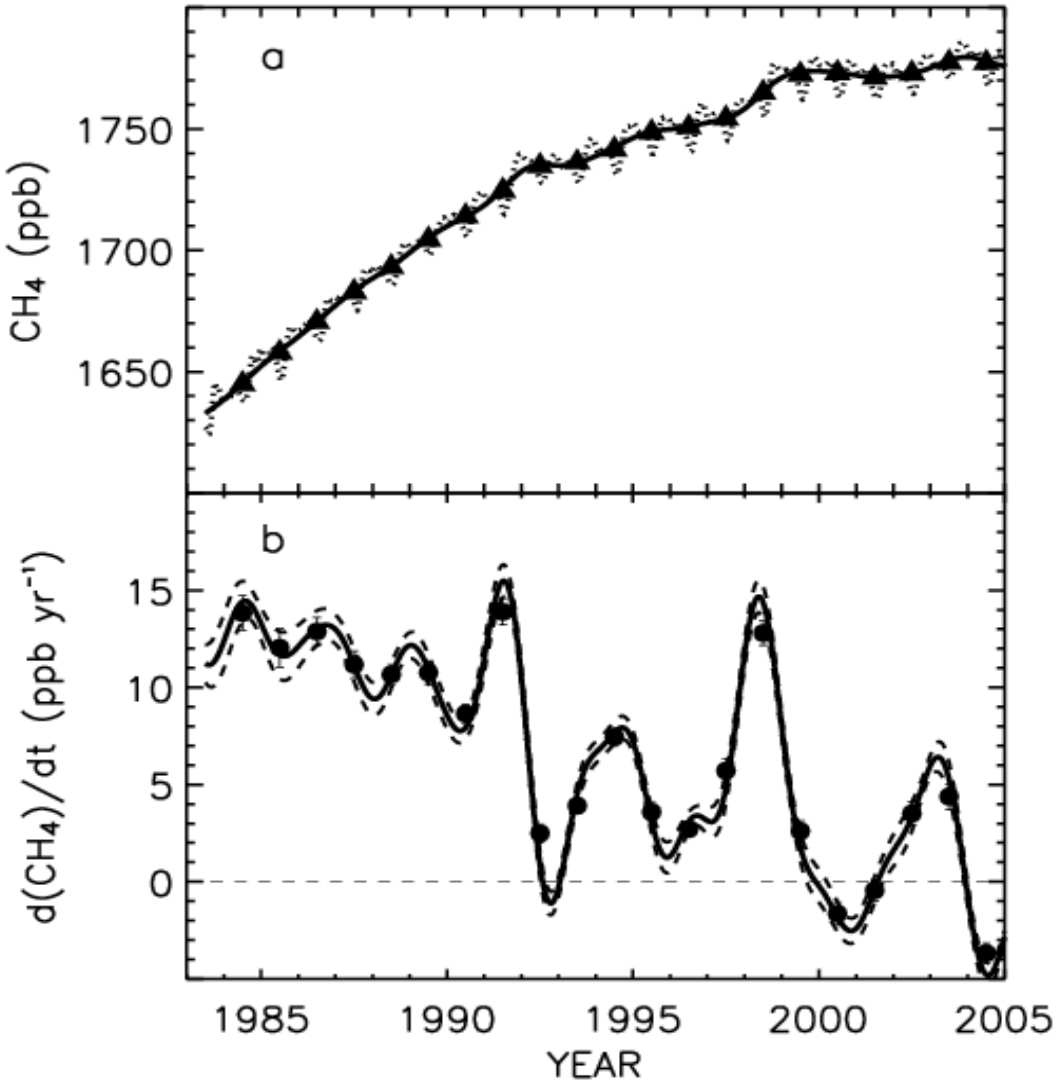

Figure 2.3.4. (a) Change in global methane abundance (mole fraction in ppb) derived from surface sites operated by NOAA/CMDL. (b) Instantaneous annual growth rate (ppb yr^{-1}) in global atmospheric methane abundance from 1984 through 2004 calculated as the derivative of the deseasonalized trend curve in (a) above (solid line). The annual increases (solid circles) are from 1 January to 1 January the following year. Uncertainties for instantaneous growth rate and annual increases are 1 sigma calculated with a Monte Carlo technique.

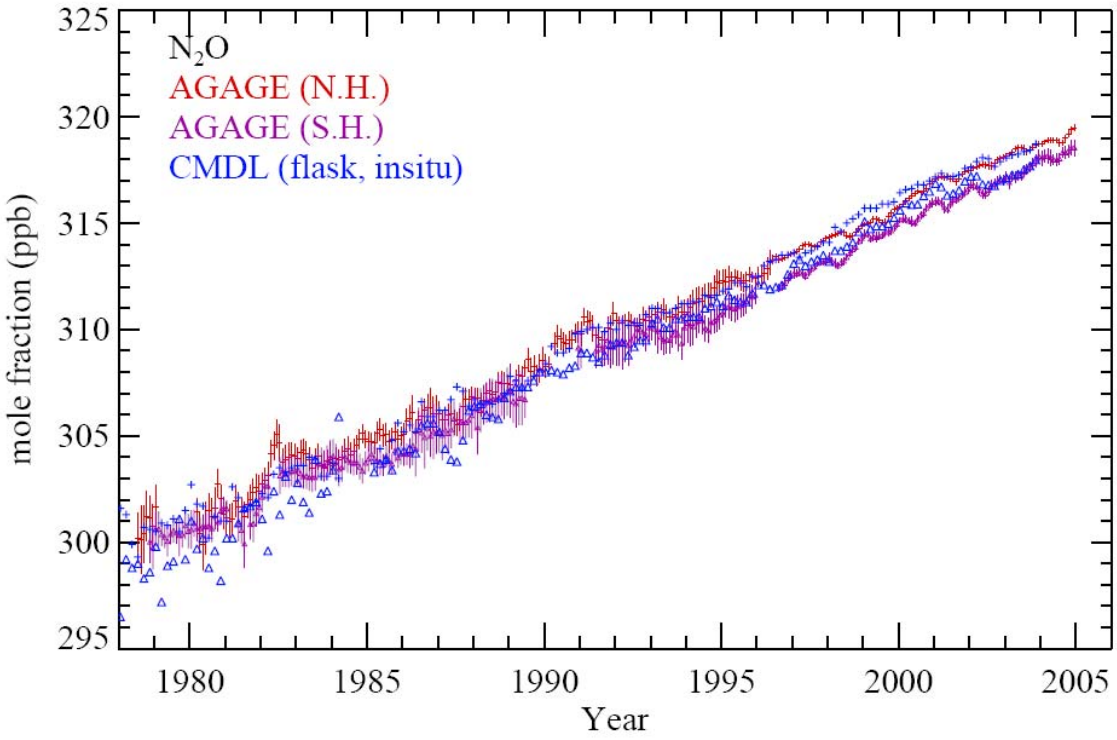

Fig. 2.3.5. Hemispheric monthly mean N_2O mole fractions (crosses for northern and triangles for Southern Hemisphere). Observations (*in-situ*) of N_2O from ALE and GAGE (through mid-1990s) and AGAGE (since mid-1990s) (Prinn *et al.*, 2000; Prinn *et al.*, 2005b) are shown with monthly standard deviations. Data from CMDL are shown without these standard deviations (Thompson *et al.*, 2004).

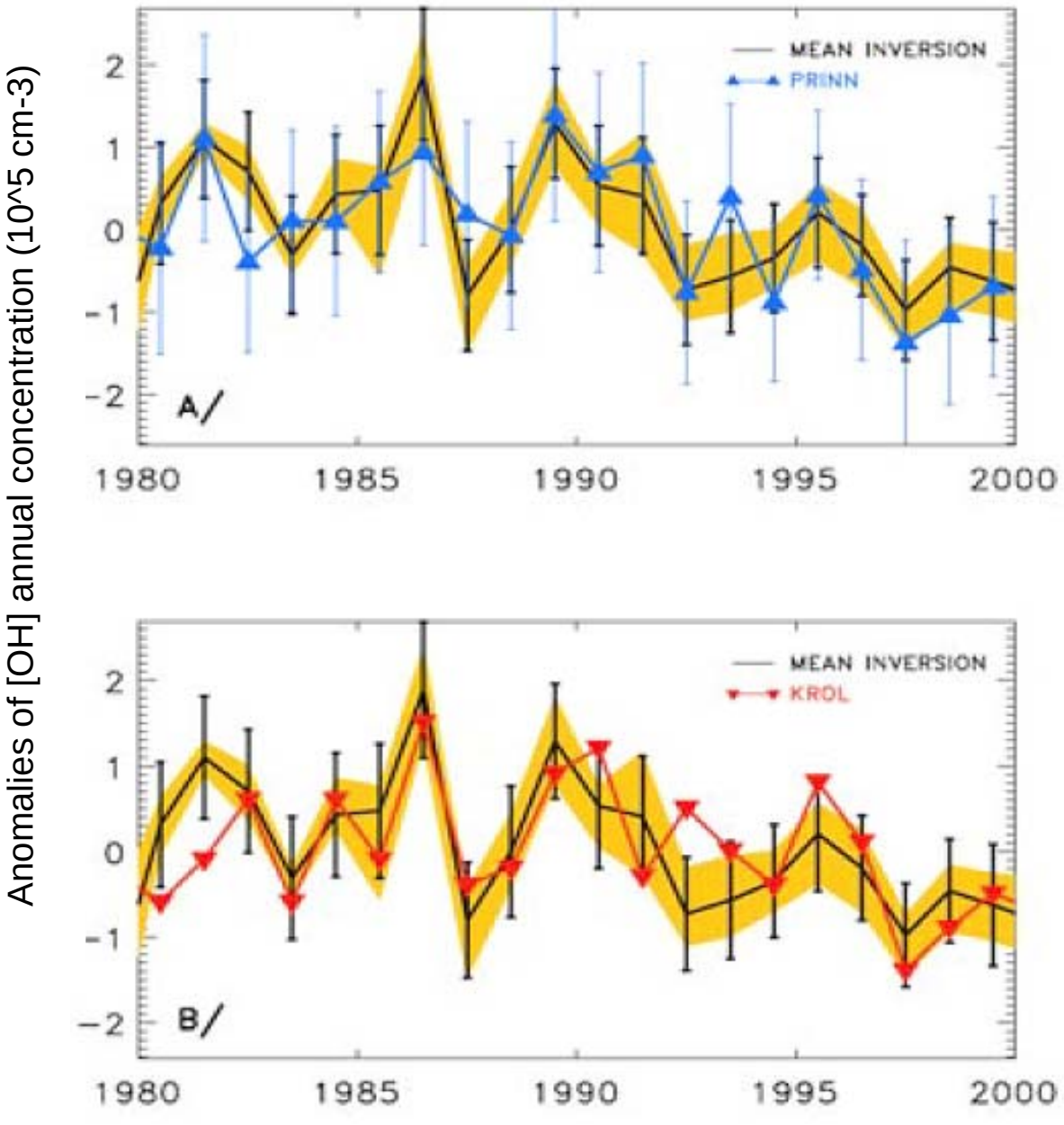

Figure 2.3.6 Annual global OH anomalies from Bousquet *et al.* (2005). Mean inversion (solid line) and envelope of all 18 inversions (yellow area) are compared with estimates> (A) from Prinn *et al.* (2001) and (B) from Krol and Lelieveld (2003).

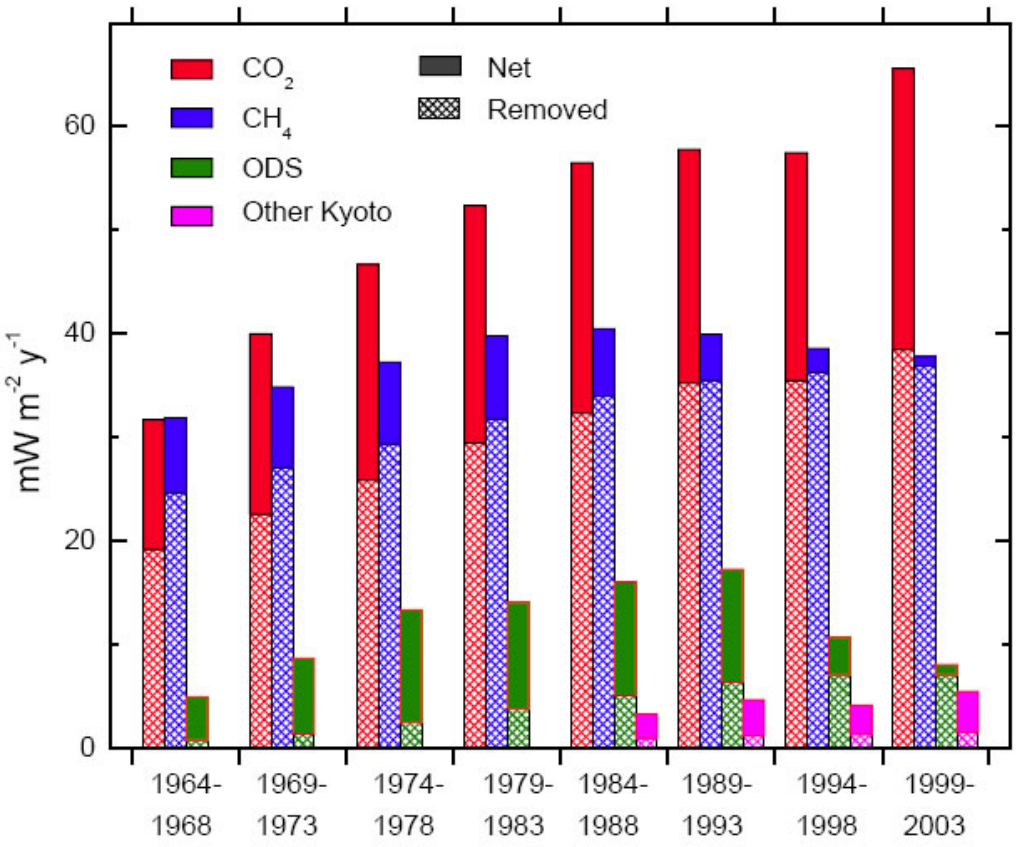

Figure 2.3.7 Annually Input Radiative Forcing (AIRF) values averaged over 8 pentads from 1964 to 2003 inclusive for CO_2, CH_4, ozone depleting substances, and other Kyoto Protocol gases as discussed in the text. Solid bars indicate the net radiative forcing for the period, whereas hatched bars represent removed radiative forcing. The total height of the bar is the AIRF value. In order to identify the effect of emissions on radiative forcing AIRF compares the radiative forcing due to an actual change in abundance of a particular greenhouse gas with the radiative forcing that would have occurred in the absence of anthropogenic emissions. It uses the estimated removal rates for the gas to infer the reduction in concentration and radiative forcing that would occur in the absence of emissions over the period of a year (from Manning, 2005).

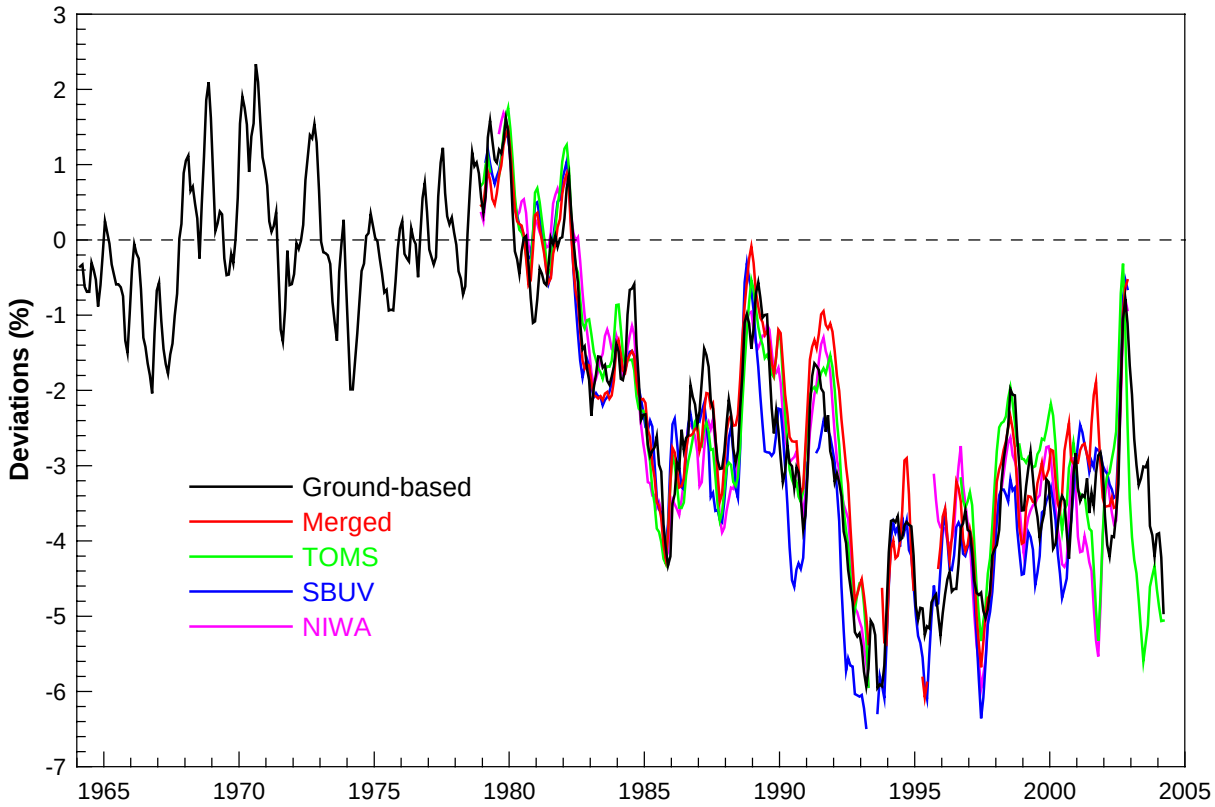

Figure 2.3.8. Time series of deseasonalized global mean total column ozone anomalies estimated from five different data sets both ground-based (black line) and satellite-based (coloured lines) measurements are included. First the seasonal cycle is removed from each data set, and the deviations are then area-weighted and expressed as anomalies with respect to the period 1964–1980. Updated from Fioletov *et al.* (2002).

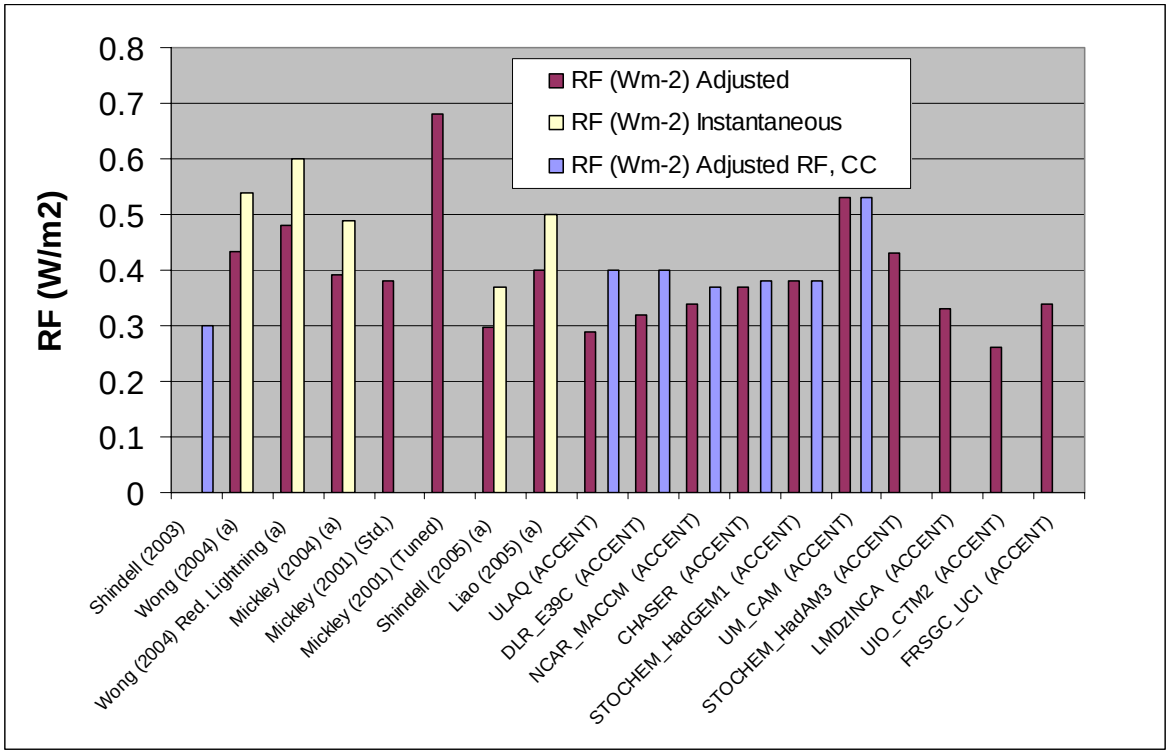

Figure 2.3.9. Calculated radiative forcing due to tropospheric ozone change since pre industrial time based on CTM and GCM model simulations published since the TAR. Estimates with GCMs including the effect of climate change since 1750 are given by the blue bars (Adjusted RF, CC). Studies donatedwith an (a) give only instantaneous RF. Adjusted RF for these are estimated by reducing the instantaneous RF by 20%. The instantaneous RF from Mickley *et al.* (2001) is reported as adjusted RF in Gauss *et al.* (2005).

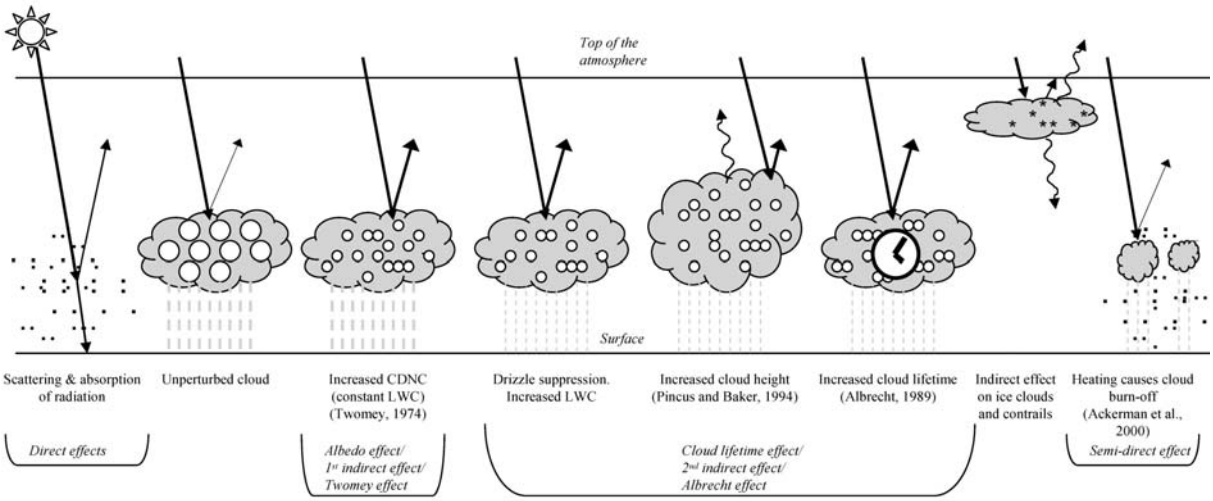

Figure 2.4.1. Schematic diagram showing the various radiative forcing mechanisms that have been identified as significant (modified from Haywood and Boucher, 2000). The small black dots represent aerosol particles, the larger open circles cloud droplets. Straight lines represent the incident and reflected solar radiation and wavy lines represent terrestrial radiation. The unperturbed cloud contains larger cloud drops as only natural aerosols are available as cloud condensation nuclei (CCN, CDCN on Figure), while the perturbed cloud contains a greater number of smaller cloud drops as both natural and anthropogenic aerosols are available as CCN. The vertical grey dashes represent rainfall. LWC is the liquid water content.

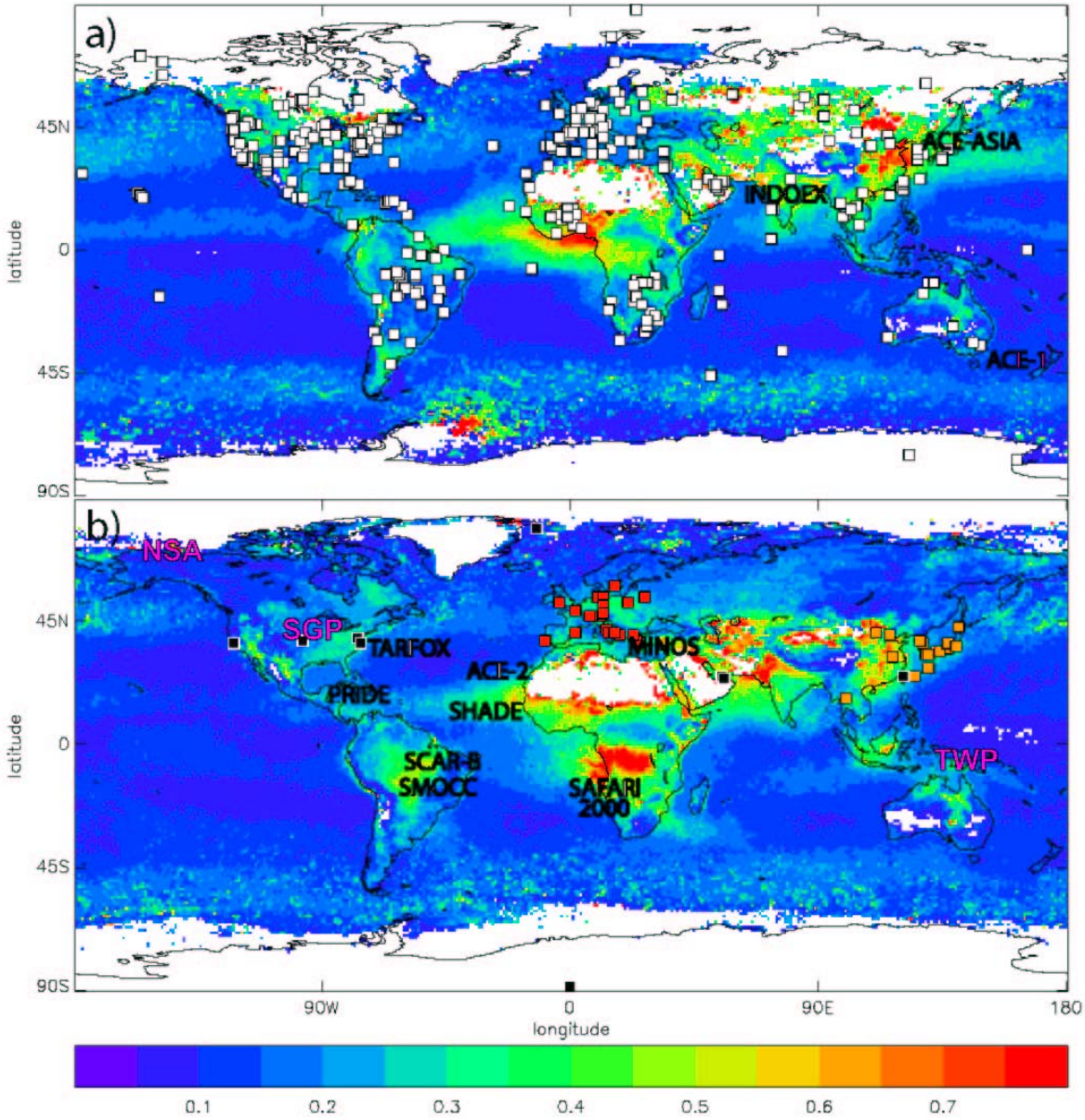

Figure 2.4.2. The τ_{aer} at 550 nm determined by the MODIS instrument for (a) January/February/March 2001, (b) for August/September/October 2001. a) Shows the location of AERONET sites that have been operated since 1996 and major international aerosol measurement campaigns carried out during the January/February/March time period. b) Shows the location of different aerosol lidar networks (red = EARLINET, orange = ADNET, black = MPLNET) and major international campaigns carried out during the August/September/October time period. The major international targeted aerosol campaigns are marked in black, while the ARM sites are marked in pink to distinguish between intensive campaigns and year-round sites. SGP = Southern Great Plains, TWP = Tropical West Pacific, NSA = North Slope Alaska. ACE= Aerosol Characterisation Experiment, INDOEX=INDian Ocean EXperiment, SHADE=SaHAran Dust Experiment, SAFARI-2000=Southern AFricAn Regional science Initiative-2000, PRIDE= Puerto RIco Dust Experiment, MINOS=Meditteranean InteNsive Oxidant Study, SMOCC= SMOke Aerosols, Clouds, Rainfall and Climate, SCAR-B= Smoke Clouds And Radiation – Brazil.

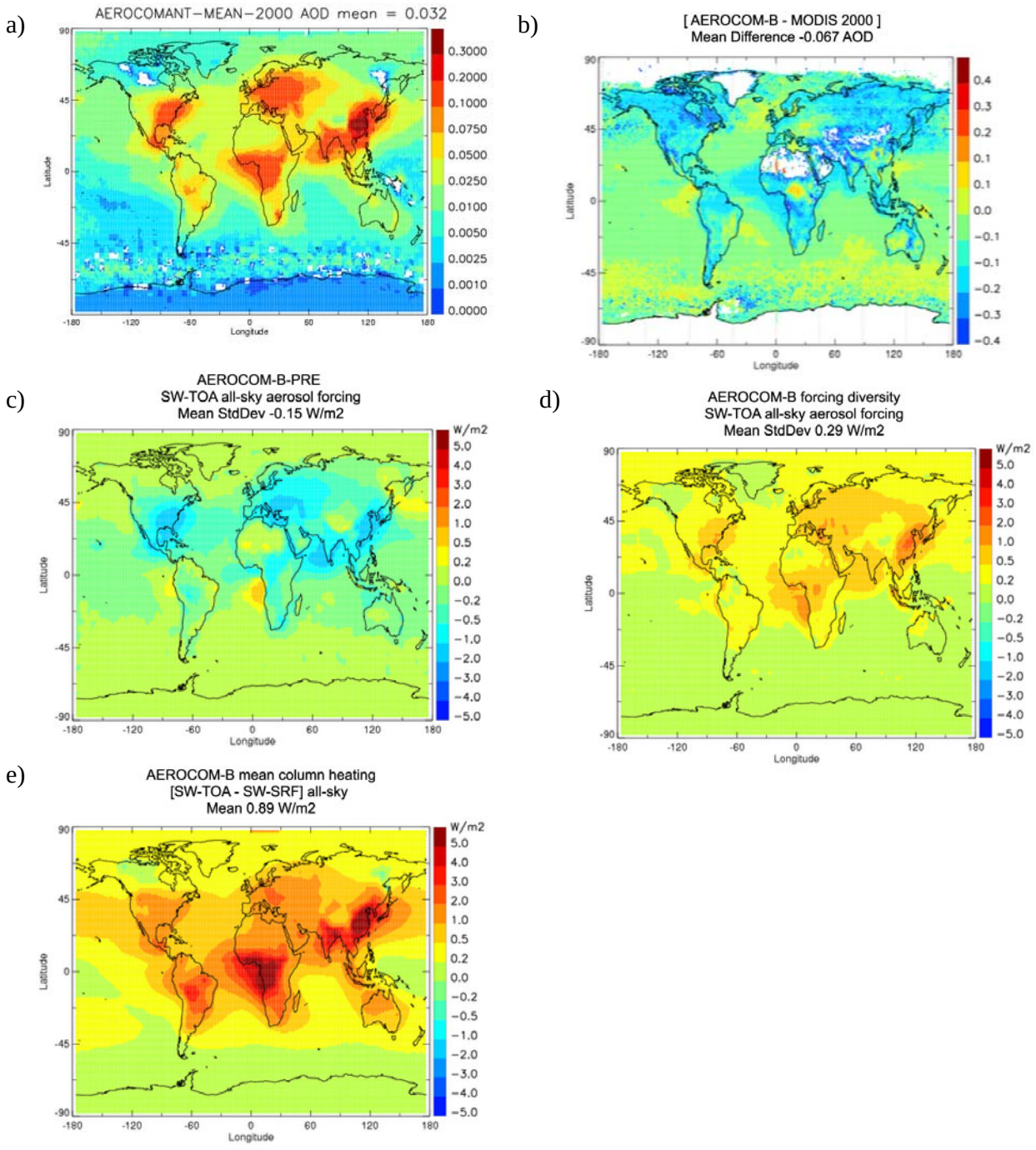

Figure 2.4.3. a) Mean anthropogenic aerosol optical depth derived from 9 models (UIO_CTM, LOA, UIO_GCM, KYU, GISS, LSCE, UMI, MPI_HAM, ULAQ) having used AEROCOM emissions corresponding to the years 2000 and 1750. **b)** Difference in total aerosol optical depth between AEROCOM B model mean and aerosol optical depth from MODIS (over land) as described in Kinne *et al.* (2005). **c)** Mean short wave anthropogenic aerosol forcing at top of the atmosphere (Difference AEROCOM B and PRE simulations). **d)** Local standard deviation of aerosol forcing at the top of atmosphere corresponding to figure c) using the results from 9 models as mentioned above. **e**) Mean Atmospheric heating rate derived from all sky top-of-the-atmosphere and surface layer radiative forcing from the same models. [Surface forcing panel will be added.]

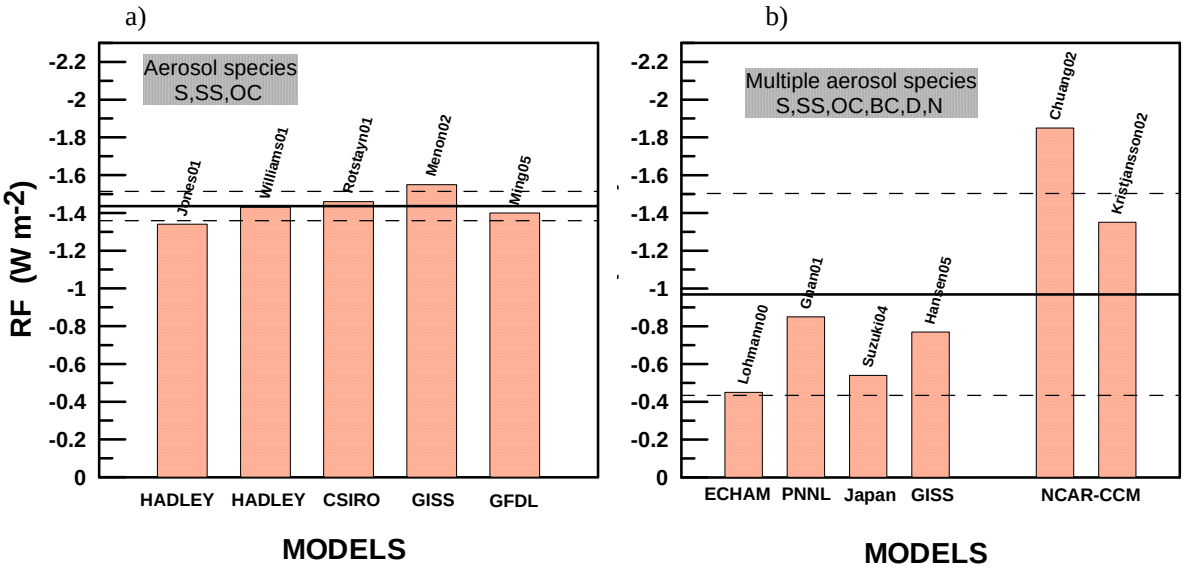

Figure 2.4.4. Albedo radiative forcing for studies that include: a) only a few aerosol species (sulphate, sea-salt and organic matter) and b) multiple aerosol species. The solid horizontal lines correspond to the averages, while the dashed lines represent 1 standard deviation. Note that in b), the average and standard deviation when only the first 4 studies are included, are: (–0.6525 ± 0.1884) W m^{-2}.Studies are described in Table 2.4.6.

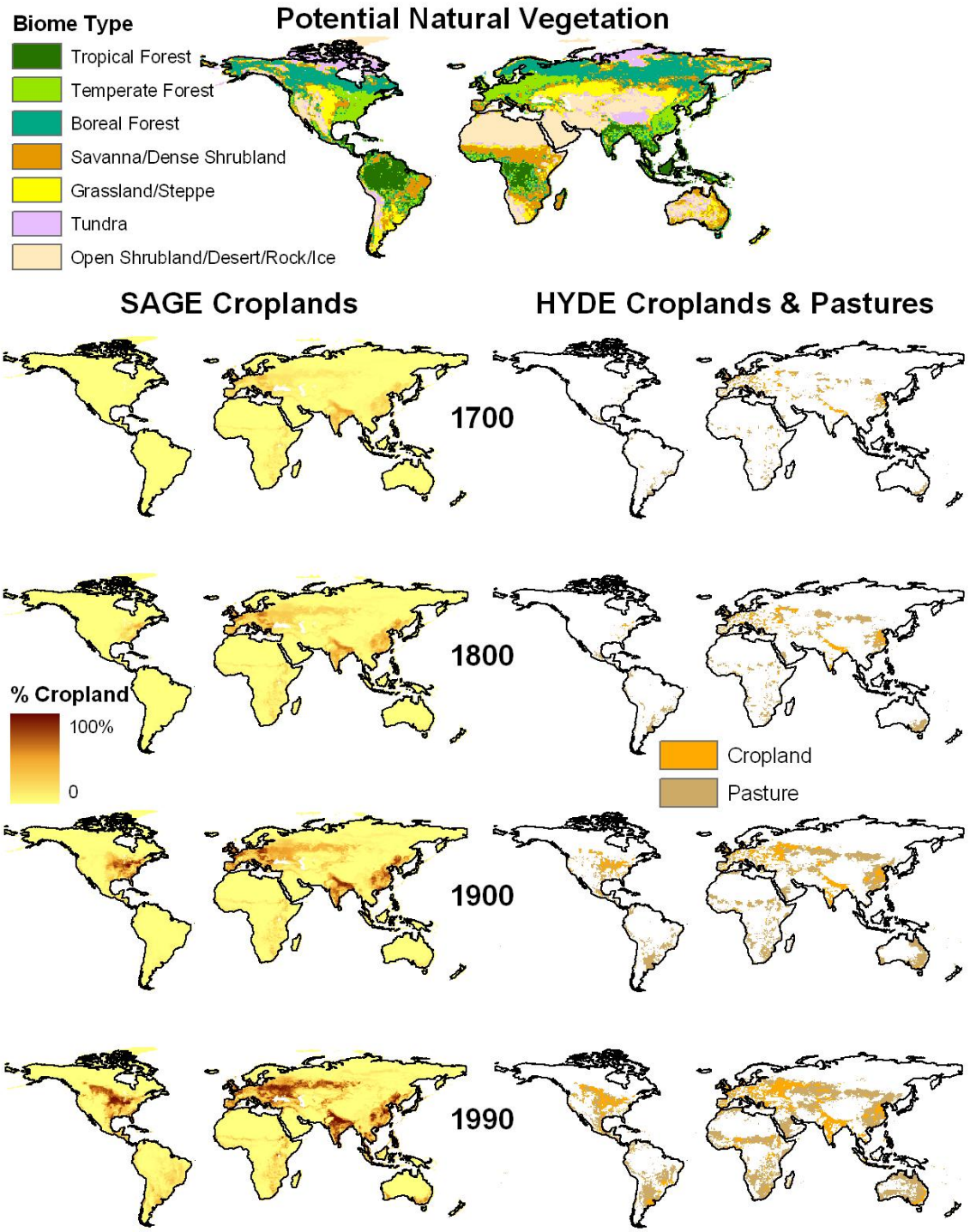

Figure 2.5.1. Maps of croplands and pasture at 1700, 1800, 1900 and 1990. Left-hand column: reconstructions from SAGE (Centre for Sustainability and the Global Environment, University of Wisconsin (Ramankutty and Foley, 1999), showing fractional cover of croplands at 0.5º resolution. Right-hand column: reconstructions from the HistorY Database of the Environment (HYDE), RIVM, Netherlands (Klein Goldewijk, 2001), with one land cover classification per 0.5º grid box.

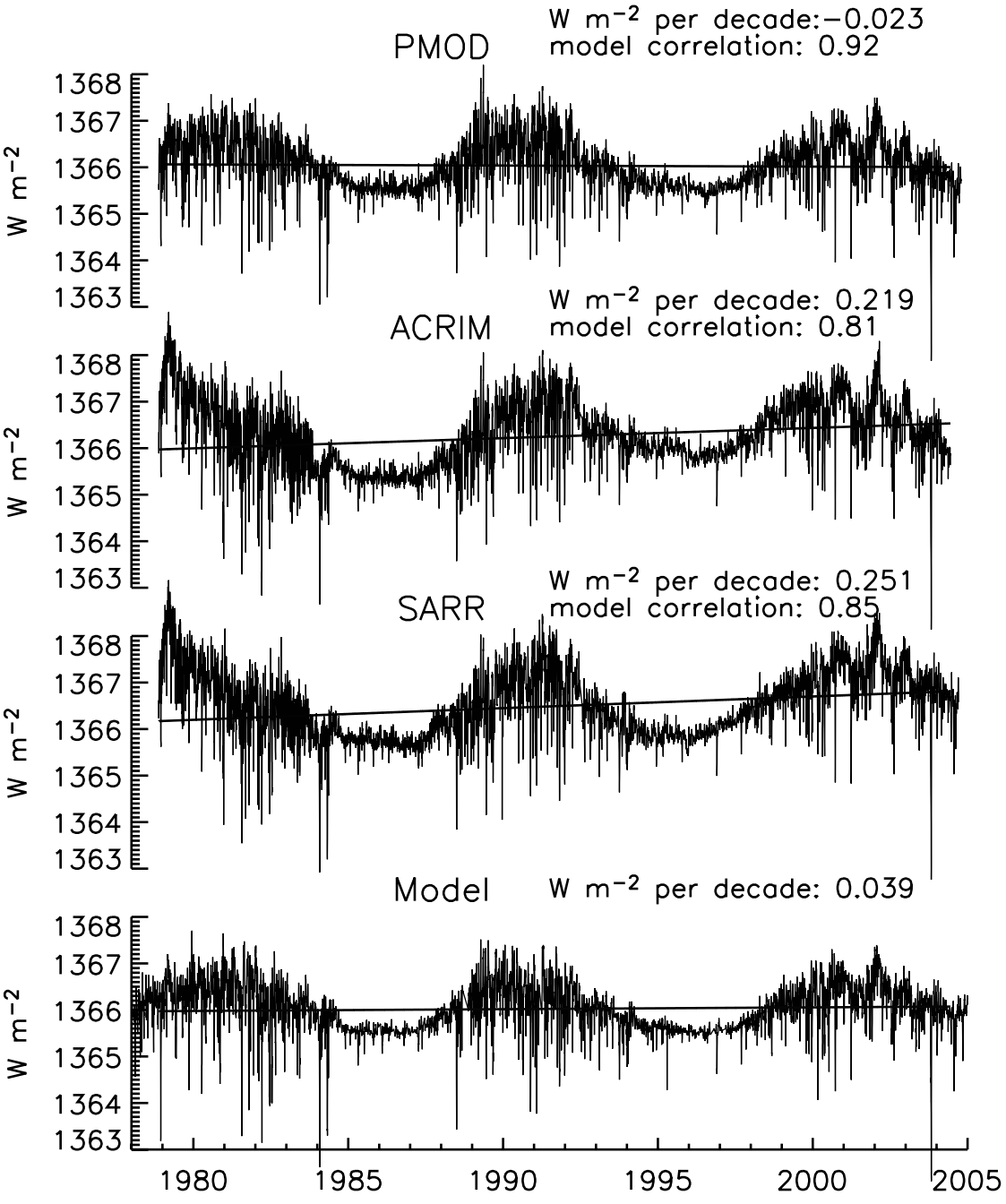

Figure 2.7.1. Shown in the upper three panels are different composite records of total solar irradiance during the era of space-based monitoring. For quantitative comparison, the slopes of the time series are computed from 7538 daily values between November 1978 and June 2004. Compared in the bottom panel is a model of total solar irradiance calculated from parameterized sunspot and facular influences (from Lean *et al.,* 2005).

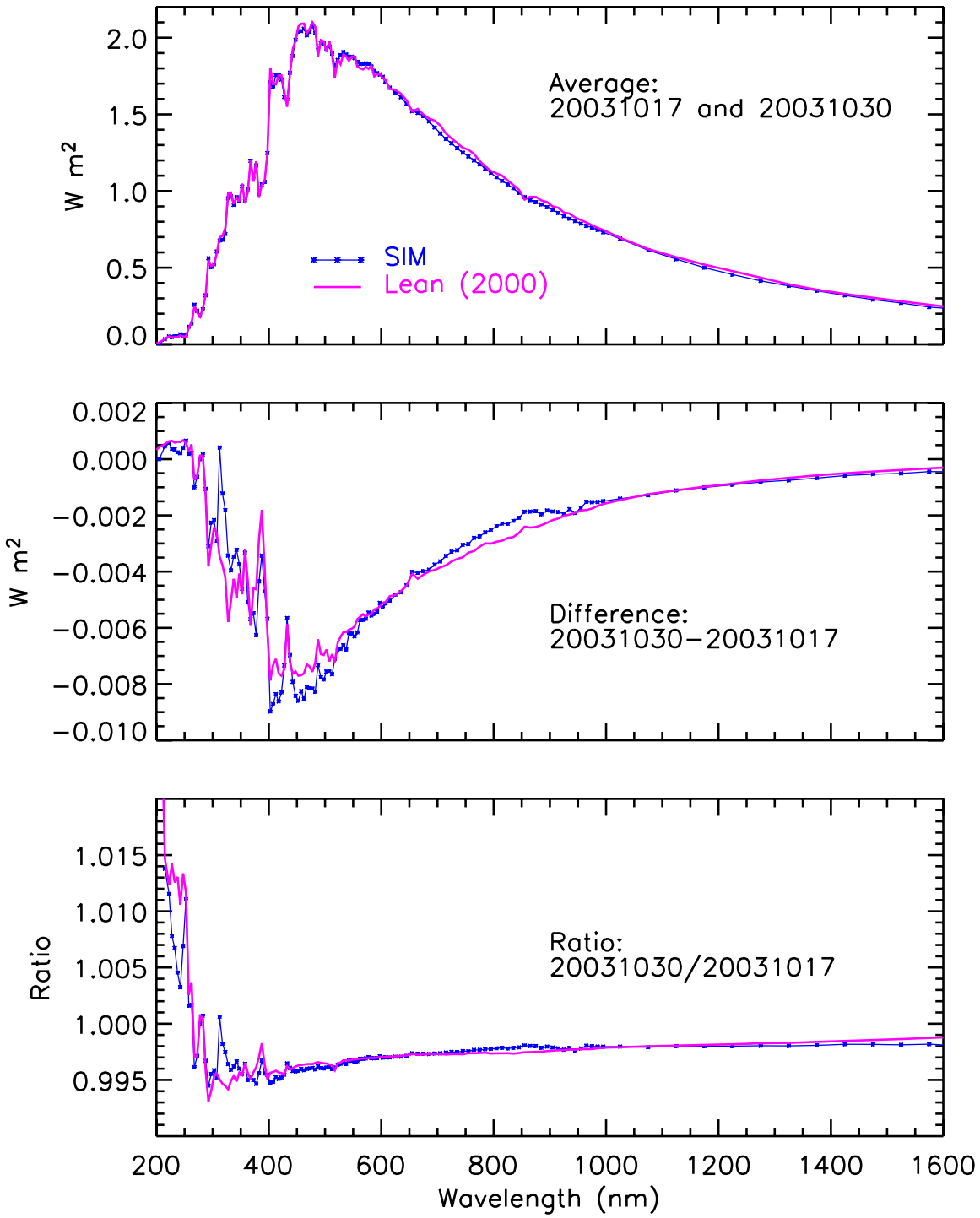

Figure 2.7.2. The solar spectral irradiance measured by SIM on SORCE, shown in the upper panel, is the average of two spectra, on 17 and 30 October 2003. Spectral irradiance changes caused by significant solar activity on 30 October, relative to quieter conditions on 17 October, are shown in the middle panel as energy differences, and the lower panel as fractional changes. A model of the irradiance variations caused by sunspots and faculae is compared with the SORCE observations.

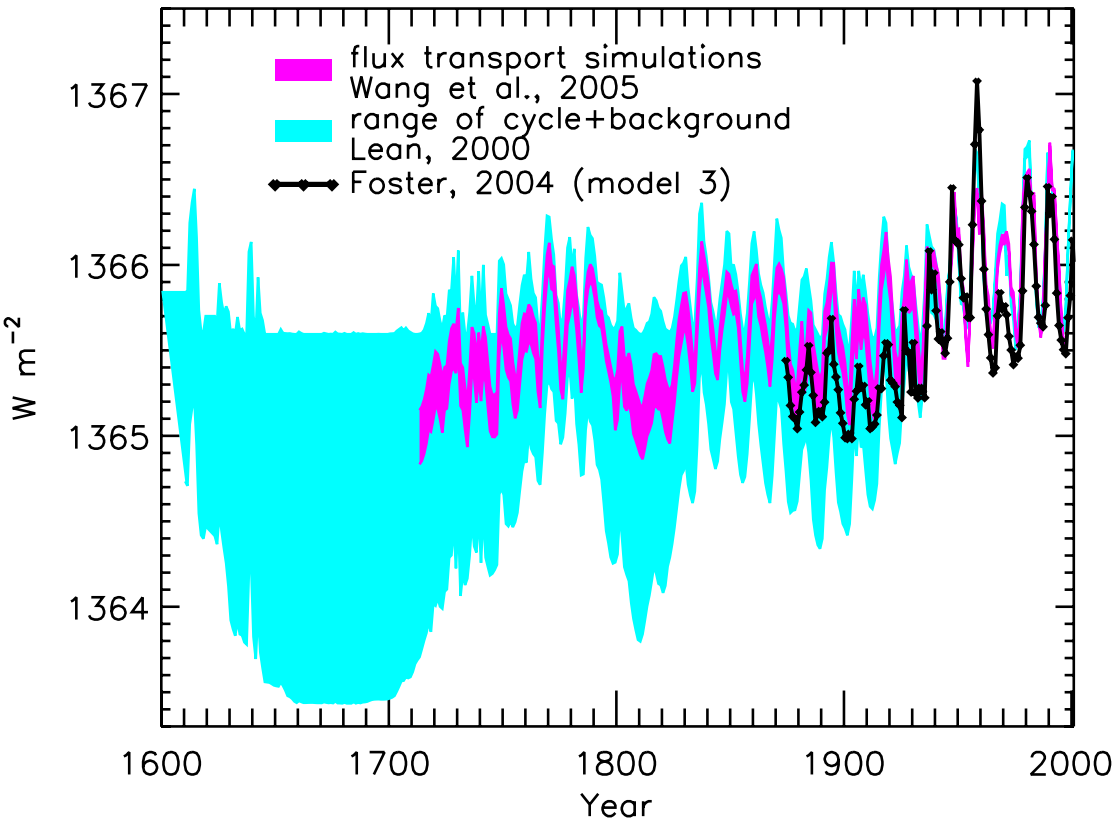

Figure 2.7.3. Shown as the upper envelope of the shaded region are total solar irradiance variations arising from the 11-year activity cycle. The lower envelope is the total irradiance reconstructed by Lean (2000), in which the long-term trend was inferred from brightness changes in Sun-like stars. In comparison are recent reconstructions based on solar considerations alone. That of Wang, Lean, and Sheeley (2005) uses a flux transport model to simulate the long-term evolution of the closed flux that generates bright faculae.

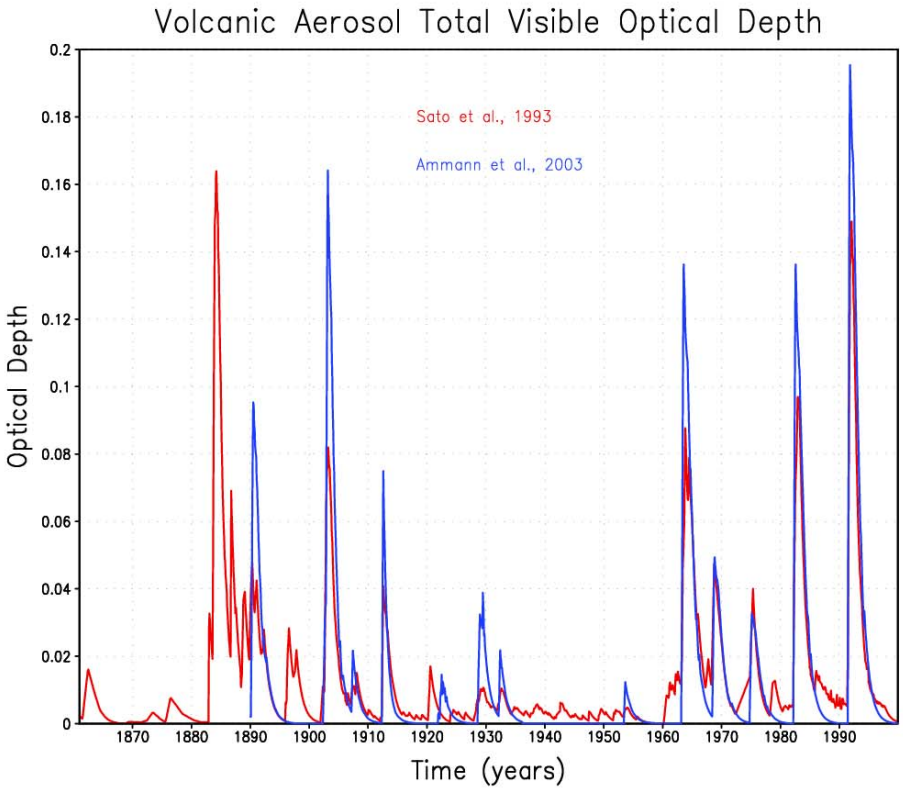

Figure 2.7.4. Visible (wavelength of 0.55 um) optical depth estimates of the stratospheric sulfate aerosols formed in the aftermath of volcanic eruptions between 1860 and 2000. Two different datasets used in recent climate model integrations are plotted.

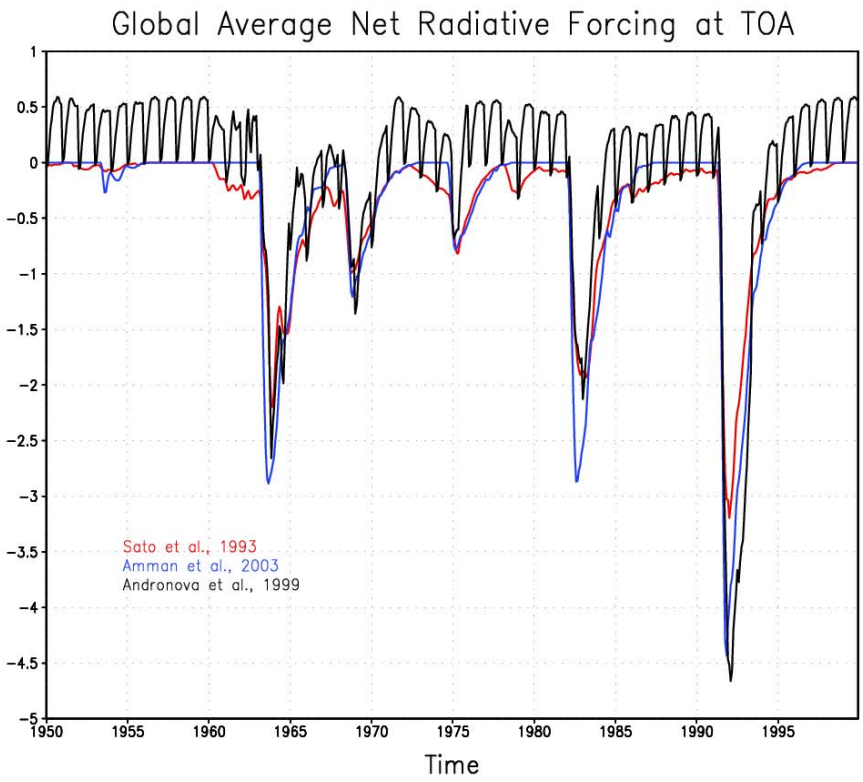

Figure 2.7.5. Global-and-annual-mean net radiative forcing at the top- of-the-atmosphere (TOA) due to stratospheric sulfate aerosols following volcanic eruptions between 1860 and 2000. Estimates resulting from 3 different datasets are shown. [Figure will be replaced for second draft.]

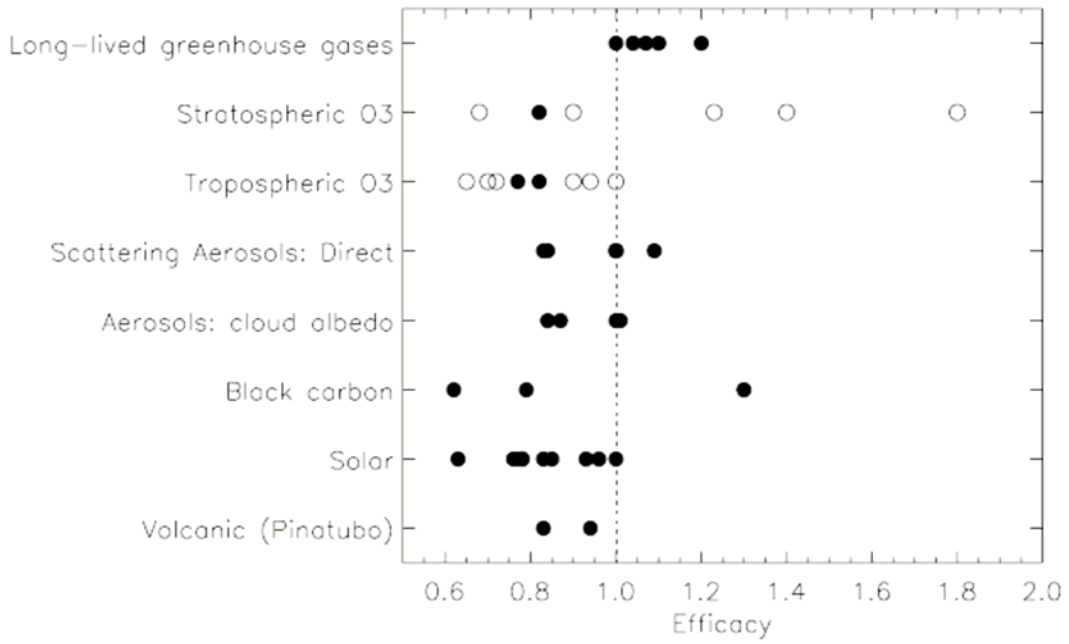

Figure 2.8.1. A synthesis of efficacies in the literature as calculated by several GCM models (Wang *et al.,* 1991; Wang *et al.,* 1992; Cox *et al.,* 1995; Hansen *et al.,* 1997; Ramaswamy and Chen, 1997; Christiansen, 1999; Forster *et al.,* 2000; B. Govindasamy *et al.,* 2001; Rotstayn and Penner, 2001; Stuber *et al.,* 2001b; Williams *et al.,* 2001a; Joshi *et al.,* 2003; Cook and Highwood, 2004; Gregory *et al.,* 2004; Mickley *et al.,* 2004; Roberts and Jones, 2004; Berntsen *et al.,* 2005b; Forster and Joshi, 2005; Hansen *et al.,* 2005; Lohmann and Feichter, 2005; Stuber *et al.,* 2005). Forcings are shown where more than two models have calculated efficacy; only one result from each model is used. Filled circles show efficacies for realistic past changes in forcing agents and are most relevant to the forcings being discussed in this chapter. The unfilled circles represent efficacies for idealised changes in ozone that may not be so relevant to the realistic forcing (see Section 2.8.5.4).

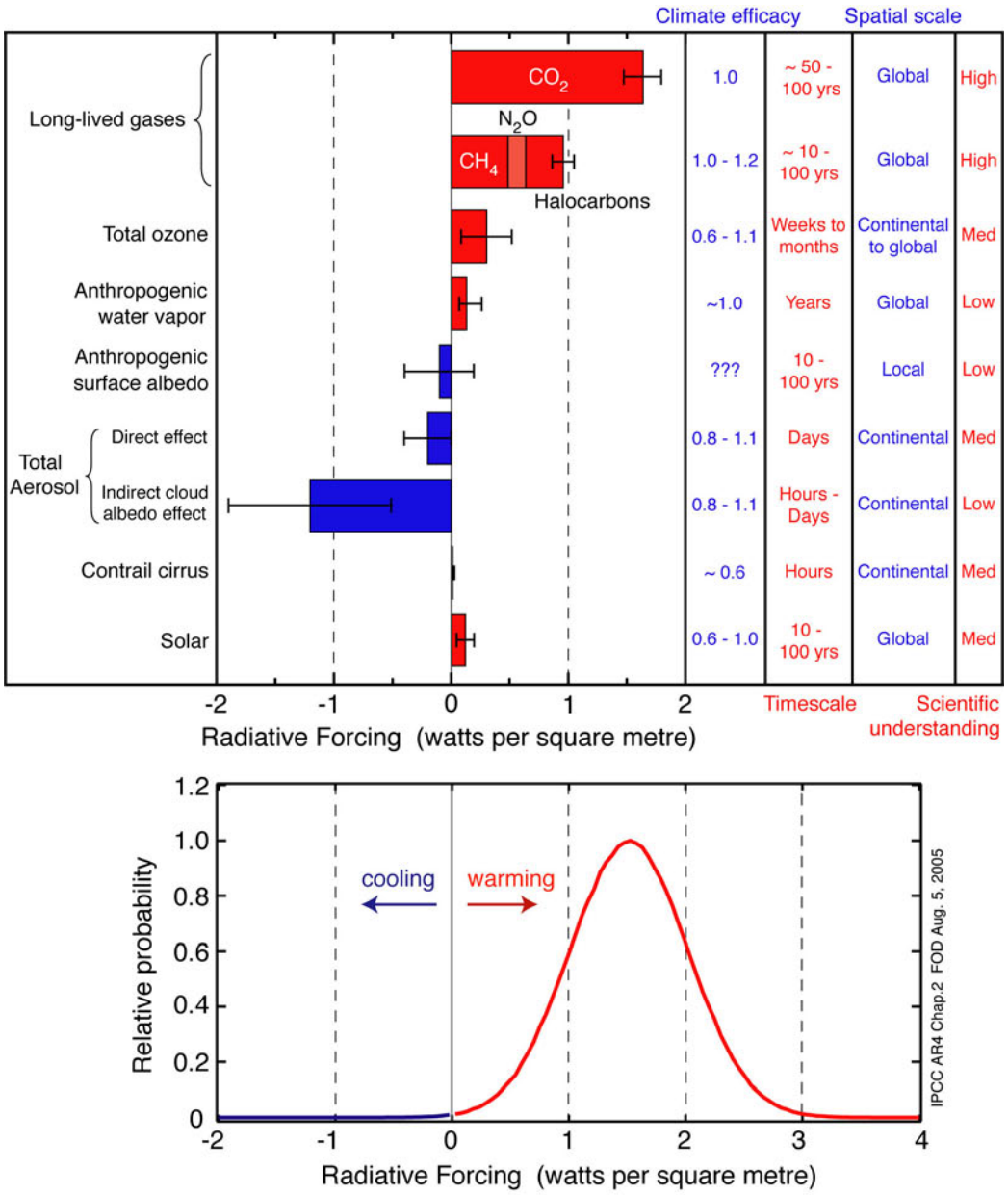

Figure 2.9.1. Top: Global mean RFs from the agents and mechanisms disused in this chapter, grouped by agent type. Columns indicate other characteristics of the RF type. Efficacies are not used to modify RFs. Bottom: Probability distribution of total global mean anthropogenic RF (no solar term), assuming uncertainty ranges on top figure correspond to 90% confidence intervals and these errors are distributed as a Gaussian. Efficacies are not accounted for. Methodology follows Boucher and Haywood (2001).

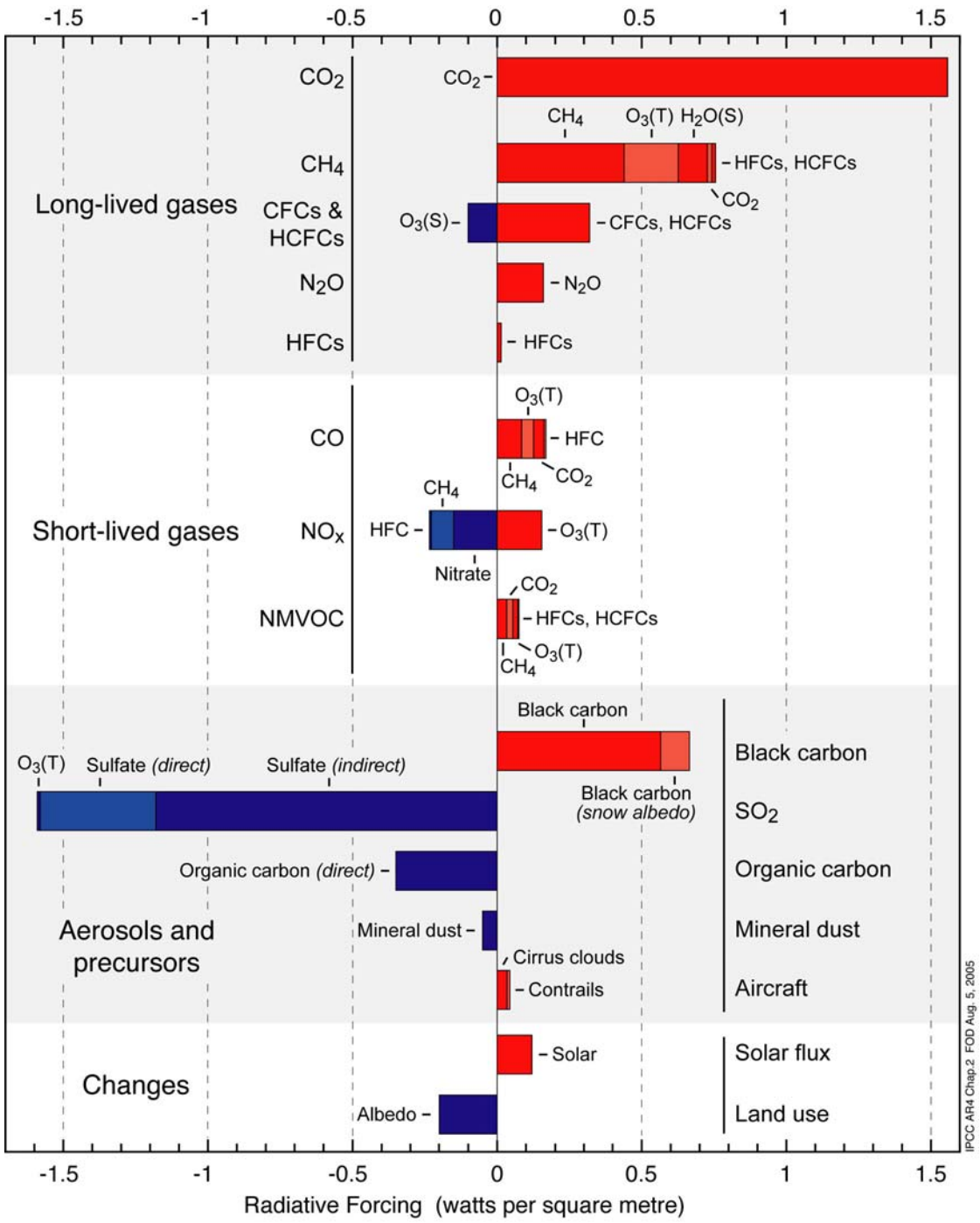

Figure 2.9.2. Components of radiative forcing for emissions of principal gases, aerosols and aerosol precursors and other changes. Values represent RF in 2004 due to emissions and changes since 1750. Only the sulphate aerosol cloud albedo RF is shown.
[Uncertainty estimates will be added to each bar. For the direct effect of the LLGHG and the aerosols this can be derived from the uncertainties of the trend analysis and RF calculations from other sections of this chapter. For the effect on tropospheric ozone and CH_4 from emissions of NO_x, CO and NMVOCs from preindustrial time, the inter model variability from the ACCENT modelling experiment (Gauss *et al.*, 2005) can be used to determine the error bars. Land use changes have given rise to a substantial fraction of the CO_2 increase and the mineral dust RF. These will be taken into account in a new version of the figure for the second draft.]

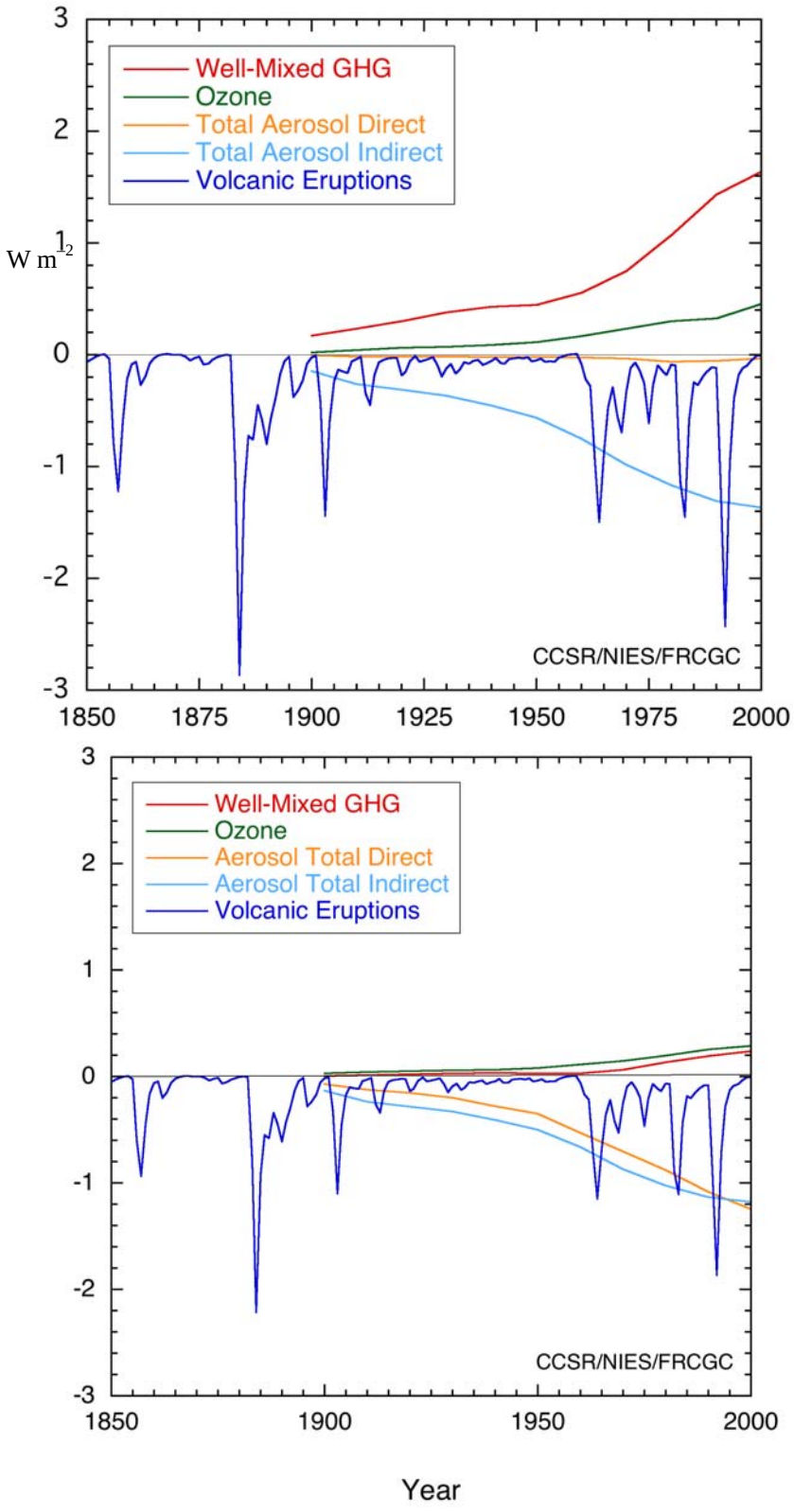

Figure 2.9.3. Globally averaged instantaneous all-sky RF (top) and surface forcing (bottom) due to various agents in the MIROC AOGCM (Takemura *et al.*, 2005).

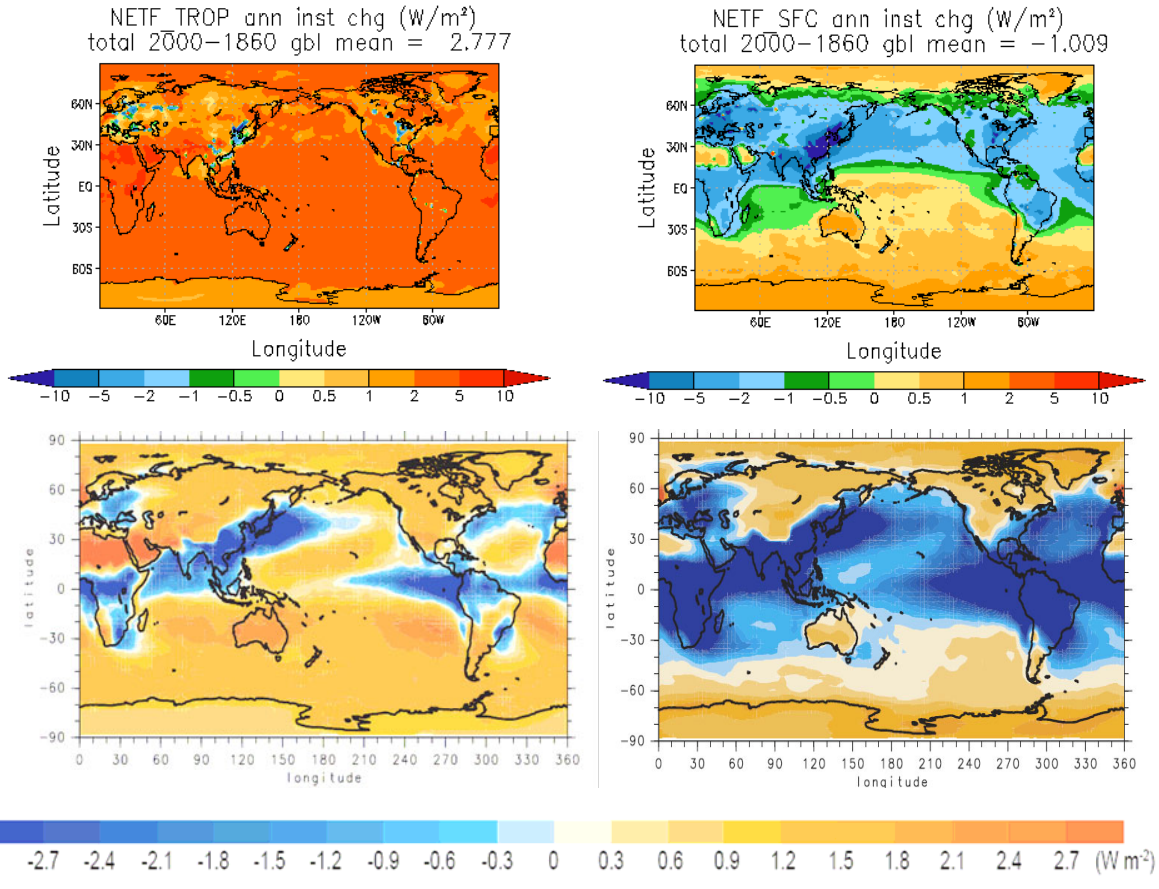

Figure 2.9.4. Spatial patterns of instantaneous RF (left) and surface forcing (right). The top panels show changes from 1860-2000 from the GFDL-CM2.1 AOGCM (Delworth *et al.*, 2005). The bottom panels show changes for 1900-2000 from the MIROC3.2 AOGCM (Takemura *et al.*, 2005). [Figure will be improved for second draft.]

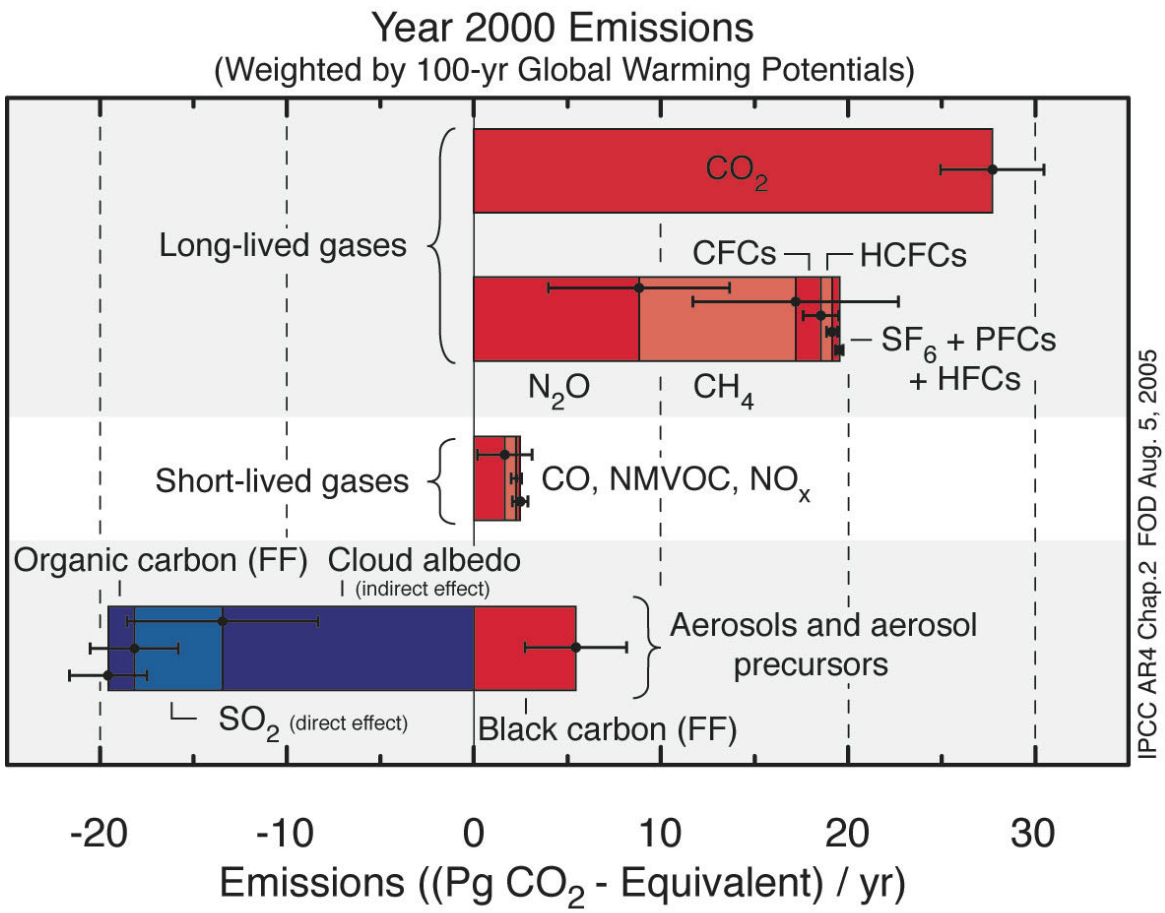

Figure 2.10.1. Year 2000 emissions weighted by 100-year GWPs. This figure is intended to be used as an indication of the future climate impact of current emissions. A number of very important caveats are associated with this figure. In particular, short-lived gases and aerosol GWPs depend critically on both when and where they are emitted. For simplicity the net GWPs are used for the ozone depleting compounds and these are unlikely to be particularly indicative of the resulting climate response – even the global mean response. The uncertainty estimates are based on both uncertainties in emission sources and the GWP estimate – these need to be carefully considered when comparing species.

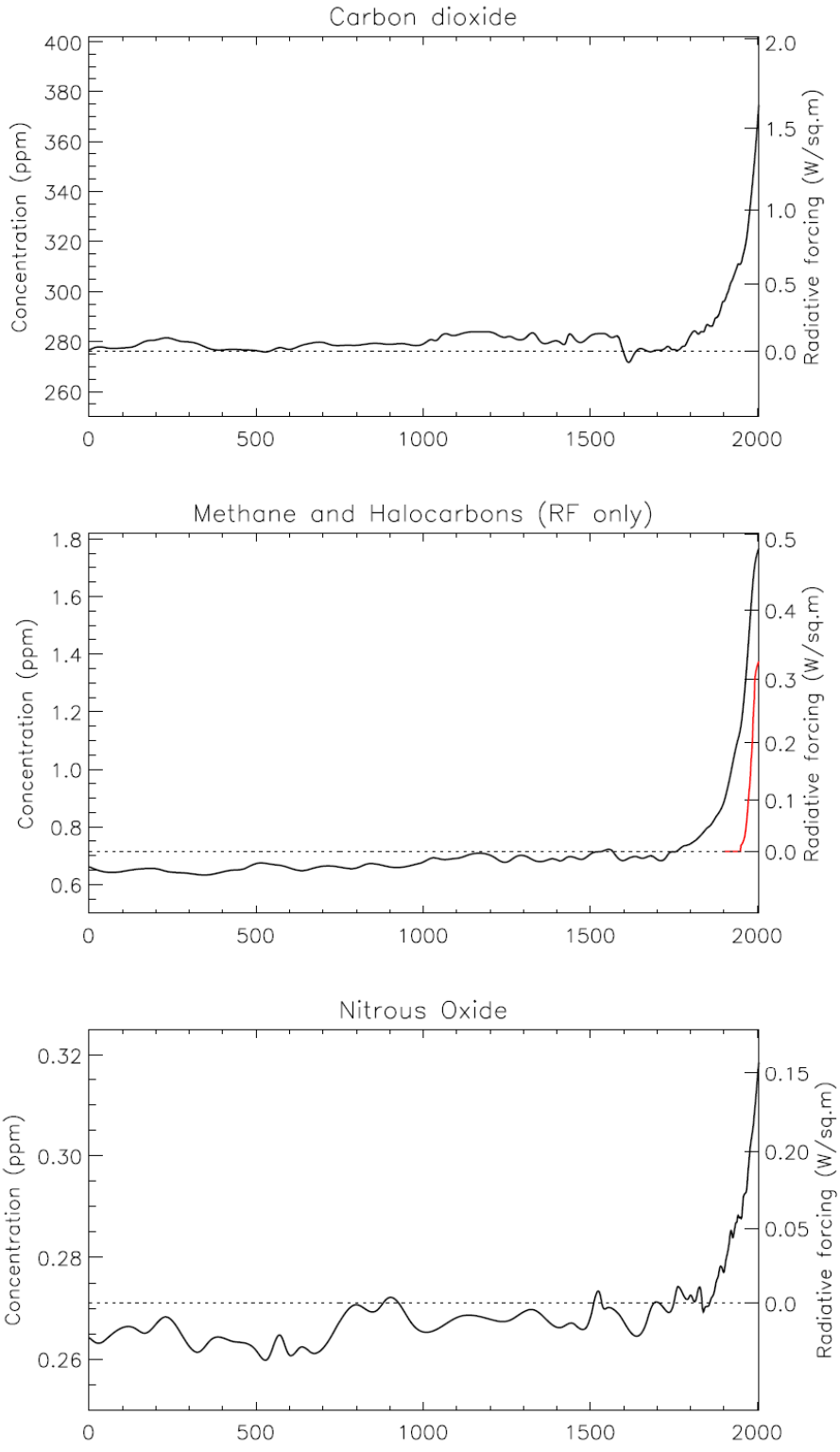

Question 2.1, Figure 1. Atmospheric amounts of three important greenhouse gases over the last 2000 years and their radiative forcing. Increases since ~1800 are attributed to human activities in the industrial era.

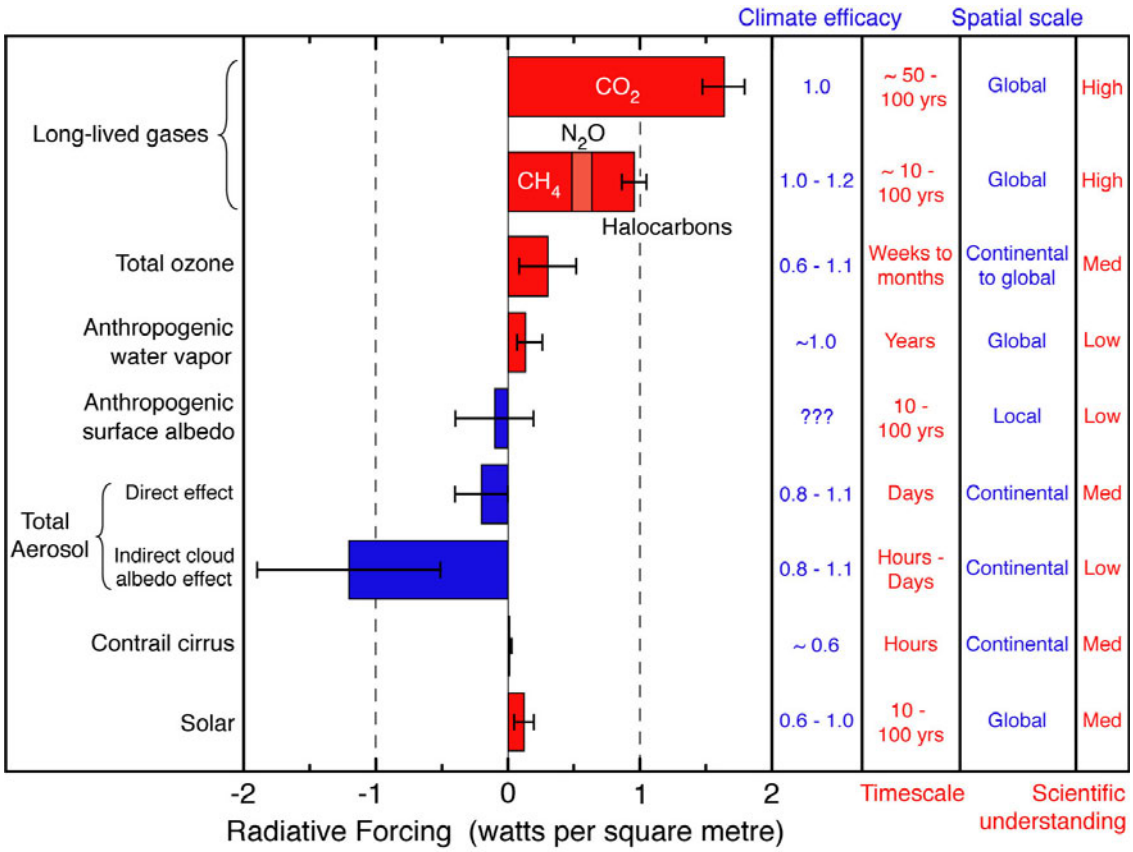

Question 2.1, Figure 2. These radiative forcings result from changes in radiative forcing agents from the start of the industrial era (about 1750) to the present (2004). Human activities cause changes in atmospheric gases, aerosols, and clouds as listed in the figure that result in either positive or negative forcings. Positive forcings lead to warming of climate and negative forcings lead to a cooling. (*Figure adopted from Figure 2.9.1 of this report.*)